# Graphitic Nanocarbon with Engineered Defects for High-Performance Potassium-Ion Battery Anodes

| Item Type | Article |
|---|---|
| Authors | Zhang, Wenli; Ming, Jun; Zhao, Wenli; Dong, Xiaochen; Hedhili, Mohamed N.; Da Costa, Pedro M. F. J.; Alshareef, Husam N. |
| Citation | Zhang, W., Ming, J., Zhao, W., Dong, X., Hedhili, M. N., Costa, P. M. F. J., & Alshareef, H. N. (2019). Graphitic Nanocarbon with Engineered Defects for High-Performance Potassium-Ion Battery Anodes. Advanced Functional Materials, 29(35), 1903641. doi:10.1002/adfm.201903641 |
| Eprint version | Post-print |
| DOI | 10.1002/adfm.201903641 |
| Publisher | Wiley |
| Journal | Advanced Functional Materials |
| Rights | Archived with thanks to Advanced Functional Materials |
| Download date | 09/08/2022 17:11:41 |
| Link to Item | http://hdl.handle.net/10754/656070 |

# Graphitic Nanocarbon with Engineered Defects for High-Performance Potassium-Ion Battery Anodes

*Wenli Zhang, Jun Ming, Wenli Zhao, Xiaochen Dong, Mohamed N. Hedhili, Pedro M. F. J. Costa, and Husam N. Alshareef\**

The application of graphite anodes in potassium-ion battery (KIB) is limited by the large variation in lattice volume and the low diffusion coefficient of potassium ions during (de)potassiation. This study demonstrates nitrogen-doped, defect-rich graphitic nanocarbons (GNCs) as high-performance KIB anodes. The GNCs with controllable defect densities are synthesized by annealing an ethylenediaminetetraacetic acid nickel coordination compound. The GNCs show better performance than previously reported thin-walled graphitic carbonaceous materials such as carbon nanocages and nanotubes. In particular, the GNC prepared at 600 °C shows a stabilized capacity of 280 mAh g$^{-1}$ at 50 mA g$^{-1}$, robust rate capability, and long cycling life due to its high-nitrogen-doping, short-range-ordered, defect-rich graphitic structure. A high capacity of 189 mAh g$^{-1}$ with a long cycle life over 200 cycles is demonstrated at a current density of 200 mA g$^{-1}$. Further, it is confirmed that the potassium ion storage mechanism of GNCs is different from that of graphite using multiple characterization methods. Specifically, the GNCs with numerous defects provide more active sites for the potassiation process, which results in a final discharge product with short-range order. This study opens a new pathway for designing graphitic carbonaceous materials for KIB anodes.

## 1. Introduction

Lithium-ion batteries (LIBs) have dominated the rechargeable battery market from the handheld devices to electric vehicles since their commercialization in 1991.[1–3] However, the scarcity and the increasing cost of lithium sources raise the concern

Dr. W. Zhang, Prof. J. Ming, Prof. P. M. F. J. Costa, Prof. H. N. Alshareef
Materials Science and Engineering
Physical Science and Engineering Division
King Abdullah University of Science and Technology (KAUST)
Thuwal 23955–6900, Saudi Arabia
E-mail: husam.alshareef@kaust.edu.sa
Dr. W. Zhao, Prof. X. Dong
School of Physical and Mathematical Sciences
Nanjing Tech University
Nanjing 211800, China
Dr. M. N. Hedhili
Core Labs
King Abdullah University of Science and Technology (KAUST)
Thuwal 23955–6900, Saudi Arabia

The ORCID identification number(s) for the author(s) of this article can be found under https://doi.org/10.1002/adfm.201903641.

about our heavy reliance on LIBs, because the cost of per round-trip energy output has become a critical consideration in emerging energy storage applications.[4–6] The need for low-cost energy storage devices motivates the paradigm transition from LIB to rechargeable batteries with earth-abundant elements.[7–10]

Although sodium-ion battery (SIB) has received great attention in the past two decades due to its similar chemistry with LIB, its commercialization is still far away.[11–14] Alternatively, potassium-ion battery (KIB) has been less explored, although KIBs possess several great advantages such as: i) low cost of potassium sources (e.g., 1000 $ per ton of potassium carbonate versus 23 000 $ per ton of lithium carbonate);[15] ii) low cost current collector, instead of copper, aluminum can be used as the anode current collector;[16] iii) K$^+$ has lower Lewis acidity leading to a smaller Stokes radius of K$^+$;[17] iv) low potential of K/K$^+$ redox couple (−2.93 V) making it possible to develop 4 V KIB.[18,19] Despite these positive attributes, the development of high-performance KIB anode has been challenging.[20–25] The successful commercial LIB anode, graphite, has a theoretical capacity of 376 mAh g$^{-1}$ with the formation of Li-saturated intercalation compound LiC$_6$. When graphite is used as the anode for SIB with carbonate-based electrolyte, the capacity of graphite is limited to 35 mAh g$^{-1}$,[26] which is a major barrier for the commercialization of SIB. The failure of graphite in SIBs has triggered the interest in the investigation of KIBs. Fortunately, potassium ions can intercalate into the graphite forming a stage I KC$_8$ compound (corresponding to a theoretical capacity of 273 mAh g$^{-1}$), which has been demonstrated in the pioneering work by Komaba et al., Luo et al., and Jian et al.[22,23,27] Various graphitic carbon materials, such as graphene, carbon nanotube, polynanocrystaline carbon, and graphitic carbon nanocages, have been investigated as anodes for KIB.[24,28–33] However, the formation of saturated stage I KC$_8$ leads to an enlargement of the (002) interlayer spacing from 0.335 to 0.532 nm corresponding to a 58% lattice expansion along the *c*-axis of graphite, much higher than in LIB (viz. 10% expansion for LiC$_6$).[15,34] The huge expansion of graphite layers makes graphite an unstable anode, which is responsible for its low rate capability and inferior cycling stability. The pursuit of

**ADVANCED
SCIENCE NEWS**
www.advancedsciencenews.com

**ADVANCED
FUNCTIONAL
MATERIALS**
www.afm-journal.de

a stable, high-capacity graphitic anode for KIB has attracted the attention of battery scientists.

Nanocarbon with ultrathin carbon layer has been demonstrated to be an effective high-performance anode of KIB. Ultrathin carbon layers enable both short K ion diffusion distances and structural integrity during (de)potassiation.[20,30,33,35,36] Nevertheless, the multiwall carbon nanotube is not suitable as KIB anode, possibly because its closed cylindrical walls are not accessible for potassium ions.[15] Creating defects in the carbon electrodes could facilitate the electrochemical reactions at the defect site.[37] On the one hand, the creation of C−C sp³ defects in graphitic carbon could provide pathways for efficient potassium ion diffusion. On the other hand, nitrogen-doping-induced defect has been demonstrated to be useful for breaking through the capacity limitation of graphite.[20,38] Nitrogen, which has a higher electronegativity than carbon, could provide extra active sites for the storage of K ions other than the spacing between graphene layers. By preparing graphitic carbon that combines high-level nitrogen doping with a certain amount of C−C sp³ defects, one could achieve high capacity, good cycling stability, and excellent rate capability.

In this work, we propose a new, facile approach for the synthesis of nitrogen-doped graphitic nanocarbons (GNCs). We prepared GNCs with controllable nitrogen-doping-induced and C−C sp³ defect densities, and lengths of graphene layers by tuning annealing temperature. The optimized GNC anode exhibits excellent electrochemical performances. A high capacity of 189 mAh g⁻¹ with a long cycle life over 200 cycles is demonstrated at a current density of 200 mA g⁻¹. Mechanistic investigations of the K⁺ uptake process reveal an interesting K⁺ storage process in our GNCs.

## 2. Results and Discussion

GNCs were prepared through annealing the ethylenediaminetetraacetic acid (EDTA) nickel coordination compound and sodium chloride mixture (the chemical structure of EDTANi·2NaCl is shown in **Figure 1**a). EDTANi·2NaCl was prepared through a coordination reaction, in which EDTA disodium salt and $NiCl_2$ react in aqueous solution. Na and Cl ions form the NaCl ionic compound crystals upon drying (verified by X-ray diffraction (XRD) in Figure S1, Supporting Information). Figure 1 illustrates the synthesis processes of GNCs. NaCl in EDTANi·2NaCl does not change during the annealing process, while the EDTANi compound is carbonized, and finally, the pyrolysis product contains nickel metal, carbon, and NaCl (Figure S2a, Supporting Information). Further, GNCs were obtained through a hydrochloric acid etching process. During the annealing process, the nickel metal inside the carbon skeleton serves as graphitization catalyst. Graphene layers grow on nickel particles and the graphitic nanobubble morphology forms (Figure 1b). Upon acid leaching, the nickel particles inside the carbon skeleton are washed off, and a hollow bubble structure forms (Figure 1c). The GNCs contain C−C sp³ and nitrogen-doping-induced defects (shown in Figure 1d,e). The hollow bubble structure is beneficial for accommodating the volume variation during (de)potassiation. The nitrogen-doped defects contribute to the pseudocapacitance and the C−C sp³
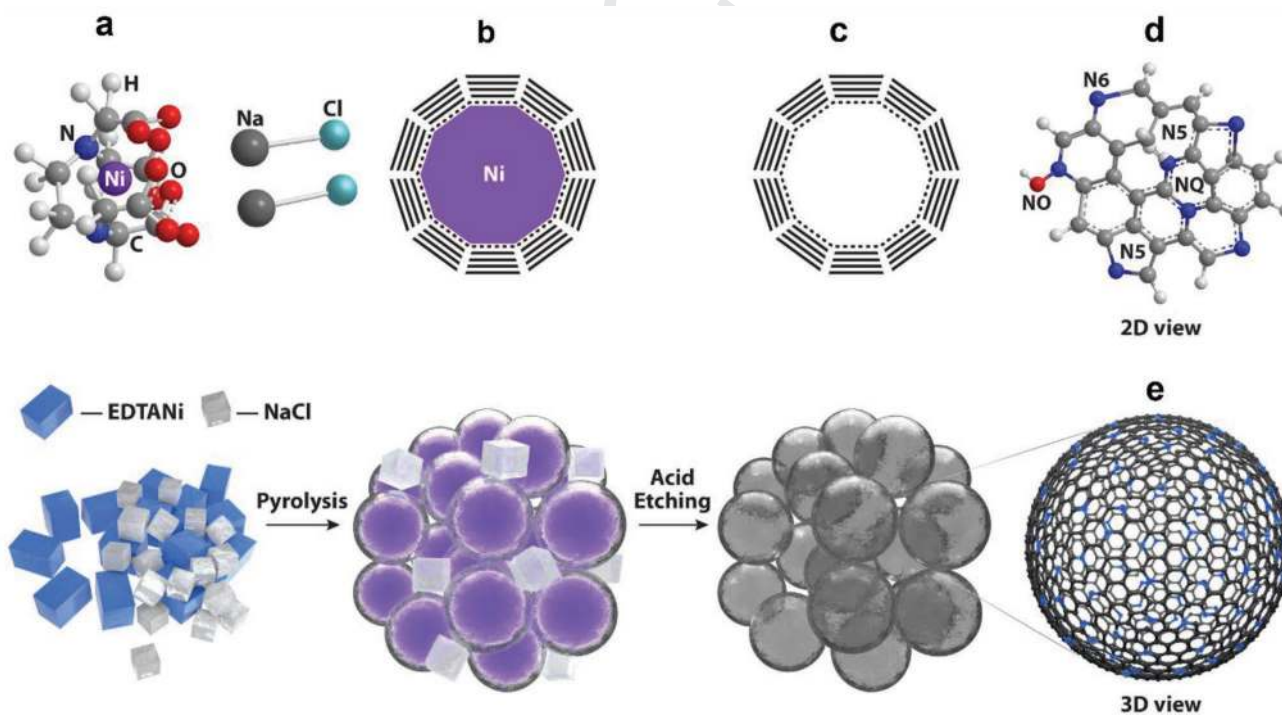


**Figure 1.** Schematic illustration of the synthesis processes of GNCs. a) Chemical structure of EDTANi·2NaCl, b) the GNC with Ni metal catalyst inside, c) the hollow structure of GNC (top: 2D view; bottom: 3D view); d) the atomic illustration of GNC with the sp³ C−C induced and nitrogen-doping induced defects, and e) the 3D view of a GNC.

**ADVANCED
SCIENCE NEWS**
www.advancedsciencenews.com

**ADVANCED
FUNCTIONAL
MATERIALS**
www.afm-journal.de

defects provide pathways for efficient K ion diffusion. The defects and graphitic structure can be tuned by changing the annealing temperature.

Annealing temperature significantly influences the morphology and structure of the pyrolysis product. With increasing temperature, the intensity of the (002) peak of graphite intensifies (Figure S2b, Supporting Information), which indicates the formation of graphitic carbon with a higher degree of crystallinity. The inner cores inside the annealing product are demonstrated to be nickel with the help of energy dispersive spectrometry (EDS) elemental mapping technique (Figure S3, Supporting Information). The sizes of nickel particles and GNC increase with temperature (Figure S4, Supporting Information).

The morphologies and structures of GNCs were analyzed through scanning electron microscopy (SEM) and high-resolution transmission electron microscopy (HRTEM) (**Figure 2**). With increasing temperature, the size of the nanocarbons increases. GNC600 has a size of dozens of nanometers (Figure 2a), GNC700 has a size of about one hundred nanometers (Figure 2b), while GNC800 has some bubbles larger than 200 nm (Figure 2c). The thickness of the carbon shells of GNC decreases (Figure 2d–f) with increasing annealing temperature. The thin carbon shells of GNCs are beneficial for fast K ion diffusion. GNC600 shows a short-range ordered graphene layer (≈10 nm) with clear disordered C—C sp³ defects (Figure 2d). The well-aligned short-range graphene layers originate from the catalytic effect of nickel, which is demonstrated by the much more disordered structure of the carbon obtained from annealing the EDTA disodium salt without nickel catalyst (Figure S5, Supporting Information). GNC700 has well-developed graphene

layers (several dozen nanometers long), and some disordered regions are found in GNC700 (Figure 2e). Although GNC800 shows the best crystalline structure, some defects still exist (Figure 2f). All the graphitic regions of GNCs show the (002) interlayer spacing of 0.340 nm, which is close to the theoretical interlayer spacing of graphite (0.335 nm).

Physicochemical methods, such as X-ray diffraction, Raman, $N_2$ adsorption/desorption, and X-ray photoelectron spectroscopy (XPS) were carried out to further clarify the structural evolution and surface chemistry of the GNCs. The XRD peaks at 26.5°, 42°, and 44° are indexed to the (002), (100), and (101) crystal planes of graphite (**Figure 3**a). The intensified (002) peak with increased annealing temperature demonstrates the increased crystal size of GNCs. No peak shift is observed for the (002) plane, which indicates an unchanged average interlayer spacing for the (002) planes. $R$-value, introduced by Dahn and co-workers,[39] was calculated from XRD patterns to quantify the defects inside the carbonaceous materials (calculation method is shown in Figure S6, Supporting Information). The $R$-values of GNC600, GNC700, and GNC800 are 2.04, 6.63, and 14.5, respectively, which demonstrates the increase of crystal size and the decrease in the density of defects in accordance with the HRTEM results.

The GNCs show coincident Raman peaks, with a D peak at 1350 cm⁻¹ induced by the defects in GNC, a G peak at 1580 cm⁻¹ induced by graphitic structure, and a 2D peak at 2700 cm⁻¹ originating from the second order zone-boundary phonons (Figure 3b). The $I_D/I_G$ ratio decreases with increasing annealing temperature (Figure 3c), demonstrating an increased degree of graphitization in agreement with the HRTEM and XRD results.
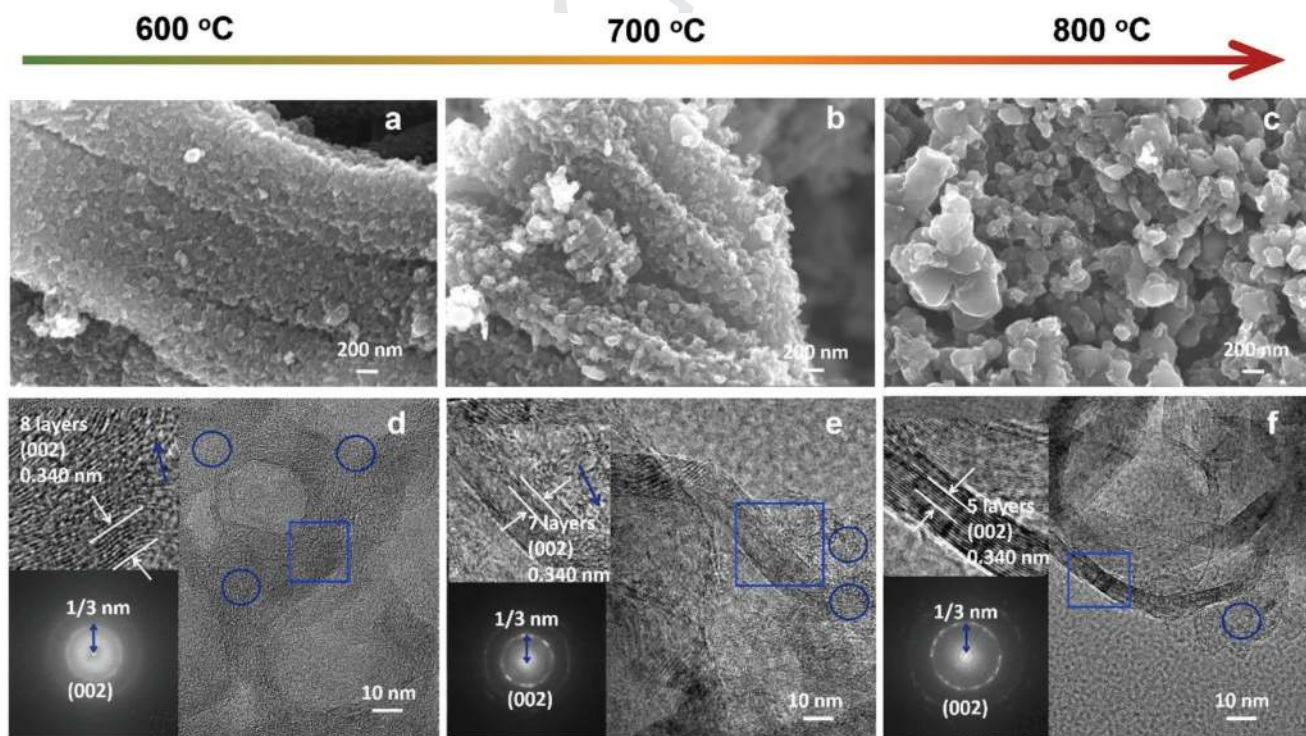


**Figure 2.** The a–c) SEM and d–f) HRTEM images of a,d) GNC600, b,e) GNC700, and c,f) GNC 800. The insets of (d), (e), and (f) are selected areas (blue squares) and their corresponding fast Fourier transform images.
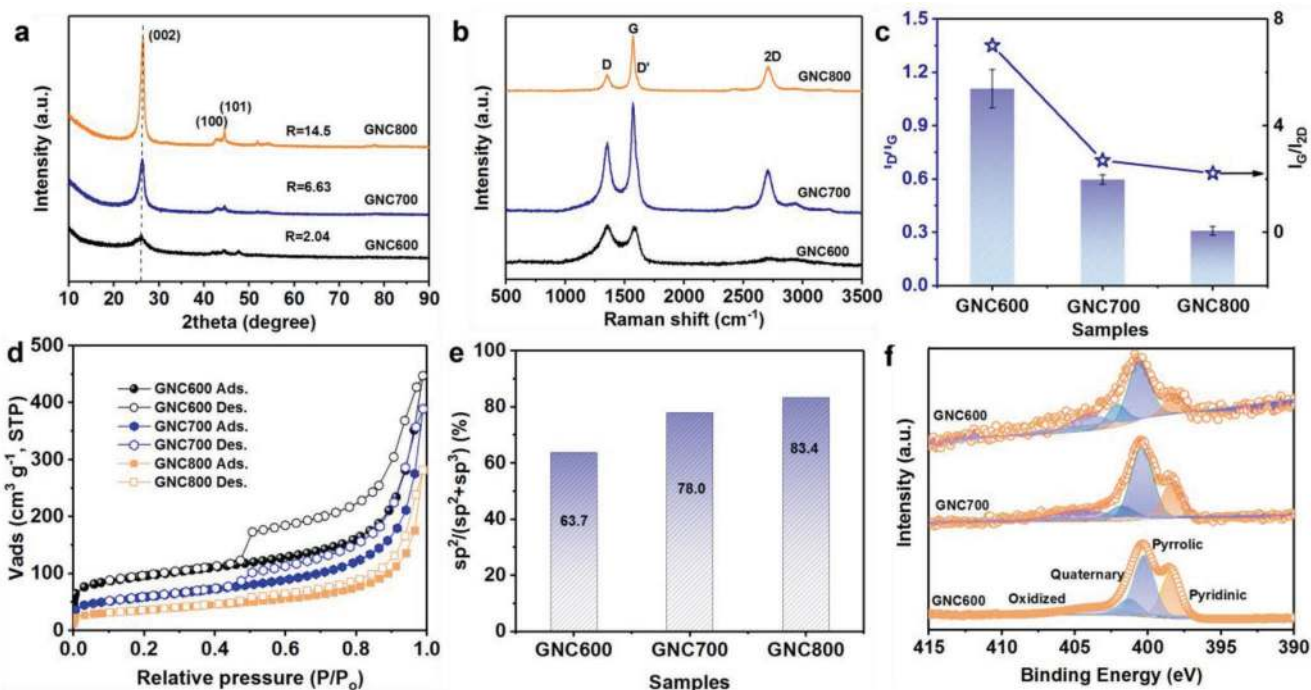
ADVANCED
SCIENCE NEWS
www.advancedsciencenews.com

ADVANCED
FUNCTIONAL
MATERIALS
www.afm-journal.de

**Figure 3.** The physicochemical properties of GNCs. a) The XRD patterns, b) the Raman spectra with c) the $I_D/I_G$ and $I_G/I_{2D}$ ratios, d) the $N_2$ adsorption/desorption isotherms, e) the $sp^2/(sp^2 + sp^3)$ ratios and f) the N 1s core level XPS spectra.

The crystal size along the $a$ axis ($L_a$) (Experimental Section S1.1, Supporting Information) increases with annealing temperature (Figure S7, Supporting Information). $N_2$ adsorption/desorption analysis was used to investigate the evolution of specific surface area and porous texture of GNCs (Figure 3d). The type IV isotherms combined with H3 type hysteresis loop demonstrate slit-shaped mesoporous textures of GNCs. The Brunauer–Emmett–Teller specific surface areas of GNC600, GNC700, and GNC800 are 305.1, 196.1, and 122.7 m$^2$ g$^{-1}$ with total pore volumes of 0.616, 0.561, and 0.419 cm$^3$ g$^{-1}$, respectively (Table S1, Supporting Information). With increasing annealing temperature, the amount of pores with size less than 40 nm decreases, while the amount of pores with the size larger than 40 nm increases (Figure S8, Supporting Information). GNC600 shows a nitrogen doping level of 4.8 at%, while GNC700 and GNC800 show nitrogen doping levels of 1.7 and 0.6 at%, respectively (Figure S9, Supporting Information). Annealing temperature is a critical factor for controlling the nitrogen doping level of GNCs. High annealing temperature leads to low nitrogen doping, which agrees well with previous publications on other forms of nitrogen-doped carbon.[36]

The graphitization and the nitrogen bonding were further studied through C 1s (Figure S10, Supporting Information) and N 1s (Figure 3f) core level XPS spectra. With increasing annealing temperature, the sp$^2$ C=C contents of GNCs increase from 48.2 to 63.8 at%, while the sp$^3$ C−C contents decrease from 27.3 to 12.7 at% (Table S2, Supporting Information). The sp$^2/(sp^2 + sp^3)$ ratios for GNC600, GNC700, and GNC800 were calculated to be 63.7%, 78.0%, and 83.4%, respectively (Figure 3e). Furthermore, the GNCs possess four kinds of nitrogen bonding (Table S3, Supporting Information), including pyridinic (398.4 eV), pyrrolic (400.2 eV), graphitic

(401.2 eV), and oxidized nitrogen (403.3 eV). Pyridinic and pyrrolic nitrogen are dangling edge-nitrogen, and they possess high electrochemical activity. GNC600 shows a high-level of edge-nitrogen doping reaching up to 72.2% (Table S3, Supporting Information). The edge-nitrogen dominated doping could provide extra defect active sites for enhancing charge storage capacity by reversibly binding potassium ions with dangling nitrogen bonds.[40]

Next, the electrochemical performances of GNCs were investigated by cyclic voltammetry (CV). The cyclic voltammograms of GNCs show different shapes, suggesting that the storage mechanisms of K$^+$ in GNCs depend on their structure (**Figure 4**a; Figure S11, Supporting Information). GNC800 shows two pairs of peaks (C1, A1 and C2, A2) (Figure 4a), which are associated with diffusion-controlled Faradaic processes. The phenomenon of two pairs of peaks has only been observed in carbon nanotubes and graphitic carbon nanocages,[30,33,41] which suggests that thin-layered graphitic materials have unique potassiation process. The origin of these two pairs of peaks is discussed later. The cathodic peak at 0.7 V appeared only in the initial cycle, which is associated with the formation of solid electrolyte interface. After the first cycle, the cyclic voltammograms become overlapped, indicating the excellent reversibility in GNCs. With increasing scan rates from 0.1 to 1.0 mV s$^{-1}$, the positions of A1 and A2 shift to higher potentials and the positions of C2 and C1 shift to lower potentials (Figure 4b), which indicates that these two peaks are from diffusion-limited Faradaic reactions. We further plotted the relation between logarithms of peak currents and scan rates to calculate the $b$ values (Experimental Section S1.2, Supporting Information). The analysis shows that the A2 and C2 peaks have higher $b$ values of 0.826 and 0.885, indicative of fast
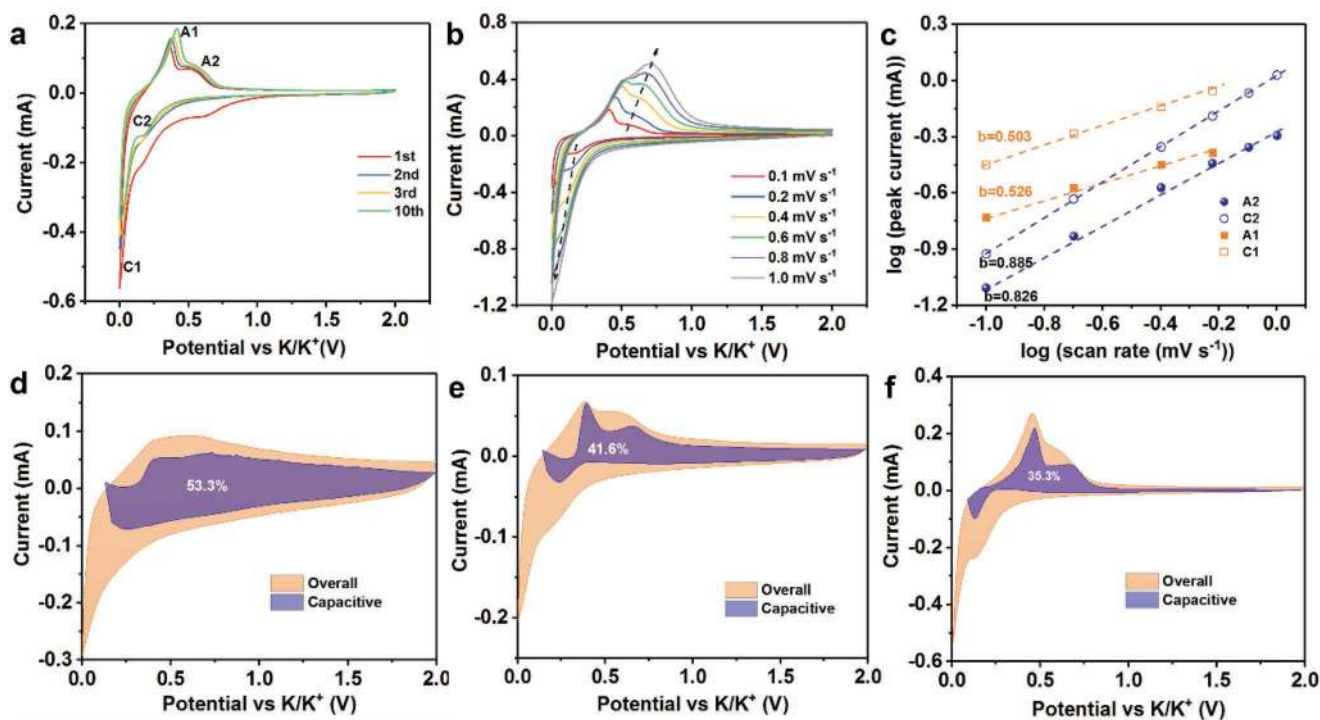
**Figure 4.** a) The cyclic voltammograms of GNC800 at 0.1 mV s$^{-1}$, b) the cyclic voltammograms of GNC800 at different scan rates, c) the logarithm relationship between the scan rates and the peak current densities, the capacitive contributions of d) GNC600, e) GNC700, and f) GNC800 at 0.2 mV s$^{-1}$.

Faradaic processes. On the other hand, C1 and A1 show *b* values of 0.503 and 0.526, respectively (Figure 4c), indicative of diffusion-controlled Faradaic behavior. The diffusion-controlled characteristic of C1/A1 indicates that the potassium ion storage mechanism is intercalation in low-potential range. However, comparing the cyclic voltammograms of GNC600 and GNC700 (Figure S11, Supporting Information), these two pairs of redox peaks of GNC800 become more clear with the formation of better graphitic structure, which further confirms that these two pairs of redox peaks originate from the potassiation in the graphite layers. The current responses of GNCs in the potential range from 0.8 to 2.0 V decrease with increasing annealing temperature, which could result from the decreased pseudocapacitive contribution originating from nitrogen doping. The Dunn method (Experimental Section S1.2, Supporting Information) was further employed to explore the potential-dependent capacitive contribution in the whole potential range from 0 to 2.0 V (Figure 4d–f). The capacitive contribution of GNC600 is 53.3%, while they are 41.6% and 35.3% for GNC700 and GNC800, respectively. The capacitive contribution in the potential range from 0.8 to 2.0 V is higher than that in the lower potential range, which demonstrates that the capacity in this range (0.8–2.0 V) is mainly due to the pseudocapacitance. Most oxygen-containing functional groups could contribute capacity at a much higher potential ($\approx$1.7 V vs K/K$^+$),[42] and GNC700 has high oxygen content but shows little capacity contribution in this range compared with GNC600. It is reasonable to conclude that the capacity contributions of GNCs in this range are mainly from the nitrogen-induced surface pseudocapacitive reactions. Judging from the cyclic voltammograms and the capacitive contribution, we could conclude that

the capacity of GNC600 mainly originates from the capacitive contribution, while the capacity of GNC800 mainly originates from the potassiation in the graphite layers. The C2 peak shows a higher capacitive contribution than C1, which demonstrates that the first potassiation process could be the preceding reaction for the second potassiation process. Both A2 and A1 show relatively high capacitive contribution, which indicates that the depotassiation process is faster than the potassiation process.

The potassium ion storage capabilities of GNCs were investigated with galvanostatic charge–discharge (GCD) at a current density of 50 mA g$^{-1}$. The initial cycles of GCD curves were plotted in Figure S12 (Supporting Information). GNCs show decreased initial Coulombic efficiencies (ICE) for GNCs prepared at higher annealing temperature, which could be due to the decreased specific surface area and defect densities. Achieving a high ICE is necessary for the assembly of a KIB full battery. The ICEs of GNCs can be enhanced by prepotassiation and surface modification. The GNC600 displays an initial charge capacity of 369 mAh g$^{-1}$, which could be due to the high nitrogen doping, agreeing with the cyclic voltammograms. GNC800 shows a high initial charge capacity of 319 mAh g$^{-1}$, which could be ascribed to the well-developed graphitic structure inside the carbon skeleton. GNC700 shows the smallest charge capacity among all GNCs, which originates from the relatively low nitrogen doping compared with GNC600 and the poorly developed graphitic structure compared with GNC800. With the clear inflection points in the GCD curves of GNC800, we divided the GCD curves of GNCs into three stages, GCD curve in the potential from 2.0 to 0.36 V (stage a), GCD curve in the potential range from 0.36 to 0.12 V (stage b), and GCD curve in the potential range from 0.12 to 0.001 V (stage c) (**Figure 5a**).
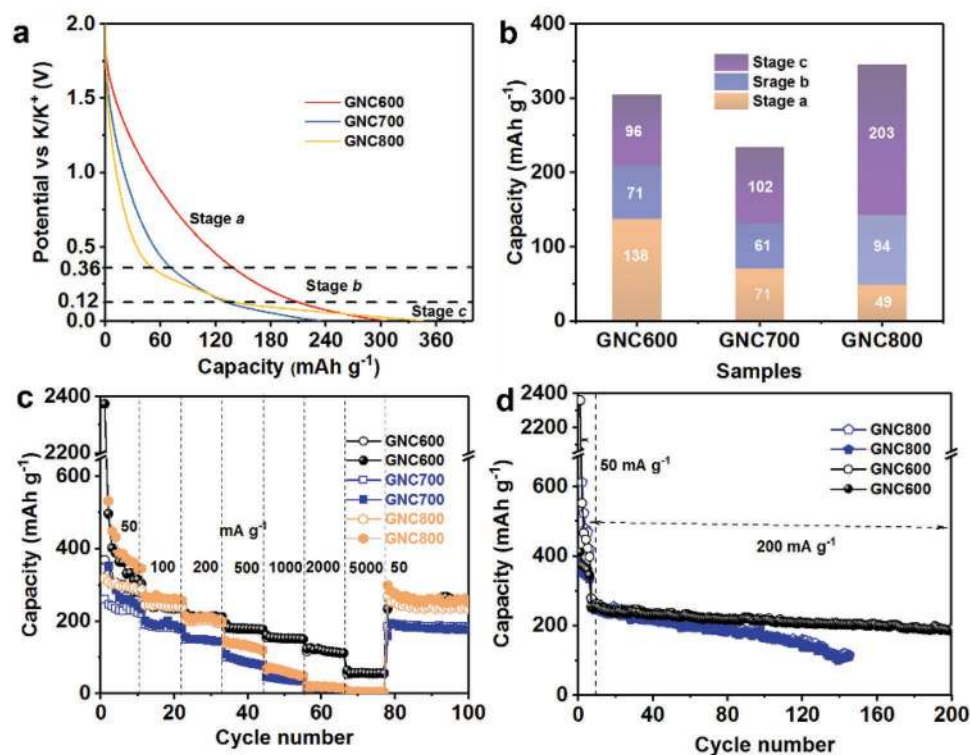
**Figure 5.** The electrochemical performances of GNCs. a) The discharge profiles of GNCs, b) the capacity contribution at each stage, c) the rate performances of GNCs, and d) the cycling stabilities of GNC600 and GNC800 at 200 mA g$^{-1}$.

These three stages show the different potential/capacity relationships (slopes), which could be due to different potassiation process. The capacities related to different stages have a clear tendency. The stage a capacity of GNCs decreases from 138 to 71 and finally to 49 mAh g$^{-1}$; the stage c capacity increases from 96 to 102 and finally to 203 mAh g$^{-1}$ with increasing annealing temperature (Figure 5b), which further proves our conclusion that the capacity of GNC600 mainly originates from capacitive contribution, while the capacity of GNC800 mainly originates from the intercalation potassiation process. The capacitive process is fast, while the Faradaic process is slow as it is diffusion-controlled. Hence, the rate capabilities of GNCs are different. The rate capabilities of GNCs are compared at different current densities from 50 to 5000 mA g$^{-1}$ (Figure 5c). The GCD curves of GNCs at different charge–discharge current densities are plotted in Figure S13 (Supporting Information). It is clear that GNC600 shows a remarkable capacity of 369 mAh g$^{-1}$, which decreases to 280 mAh g$^{-1}$ at the 11th cycle at a current density of 50 mA g$^{-1}$, while the GNC 800 displays a first charge capacity of 319 mAh g$^{-1}$ which decreases to 288 mAh g$^{-1}$ at the 11th cycle. GNC700 shows the lowest capacity of 222 mAh g$^{-1}$ at a current density of 50 mA g$^{-1}$ at the 11th cycle (Figure S14a, Supporting Information). GNC600 even shows higher reversible capacity than the delicately designed graphitic carbon nanocage,[33] porous carbon microspheres,[31] nitrogen-doped carbon fibers,[36] and nitrogen/sulfur-doped carbon (S/N@C)[43] (Figure S14b of the Supporting Information; more detailed comparisons are shown in Table S5, Supporting Information), which proves our strategy to be an efficient and easy strategy for synthesis of graphitic carbonaceous anodes for KIBs.

The GNC600 shows the best rate capability due to its surface-dominated (capacitive) potassium ion storage mechanism. GNC700 and GNC800 show inferior rate capability compared with GNC600, since the capacities of GNC700 and GNC800 mainly originate from the potassiation in graphite layers. GNC600 displays a high capacity at 152 mAh g$^{-1}$ at a current density of 1000 mA g$^{-1}$, while a high capacity of 56.6 mAh g$^{-1}$ is still maintained when the current increases to 5000 mA g$^{-1}$ (Figure 5C). On the contrary, at such high a current density, GNC700 and GNC800 show almost no capacity. The long-term cycling stabilities of GNC600 and GNC800 are compared at a GCD current of 200 mA g$^{-1}$. A preliminary activation with a low GCD current density of 50 mA g$^{-1}$ was used to activate GNCs. The coulombic efficiencies of both GNC600 and GNC800 increased to above 90% in 6 GCD cycles (Figure S15, Supporting Information). GNC600 shows superior capacity retention due to a more disordered structure inside GNC600 (Figure 5d). A high capacity of 189 mAh g$^{-1}$ is achieved at a current density of 200 mA g$^{-1}$ after GCD 200 cycles. SEM image of GNC600 obtained after cycling test shows a robust structure of GNC600 with bubble-like assembly (Figure S16, Supporting Information), which demonstrates the structural stability during (de)potassiation. GNC800 shows inferior cycling stability, which could be due to the large volume expansion/shrinkage during (de)potassiation.

Although hard carbon has been demonstrated to be an efficient anode for SIB and KIB, the storage mechanism has been difficult to understand because of the complex arrangements of short-ranged graphene layers inside hard carbon. As a result, the storage mechanism of sodium in hard carbon is still

**ADVANCED
SCIENCE NEWS**

www.advancedsciencenews.com

**ADVANCED
FUNCTIONAL
MATERIALS**

www.afm-journal.de

under debate.[44–48] For KIBs, we used the defect-rich graphitic carbons for a mechanistic study. Since GNCs both contain disordered structures and graphitic regions, we could elaborate on the different potassiation process in both amorphous and graphitic structures. In this work, we chose GNC800 as a model electrode to study the potassiation and depotassiation process. The potassiation process and depossiation process were studied by ex situ XRD, Raman, XPS, and transmission electron microscopy (TEM) techniques. First, ex situ XRD was used to prove the different potassiation stages (**Figure 6**a). The (002) peak decreases when GNC800 is discharged to 0.4 V, but no graphite potassium intercalation compound was detected, which demonstrates that most potassium ions are chemically adsorbed at the nitrogen-induced and $sp^3$ defect sites of GNC800. $KC_{24}$ starts to appear when GNC800 is discharged to 0.3 V. The peaks of $KC_{24}$ become more intense when GNC800 is discharged to 0.2 V, which indicates the further formation of $KC_{24}$. When GNC800 is discharged to 0.1 V, the peaks of $KC_{24}$ start to decrease and the peaks of stage I $KC_8$ start to appear. After GNC800 is discharged to 0 V, the pure $KC_8$ is detected. Meanwhile, a small graphitic (002) peak can be observed, which indicates that there are still some ordered graphitic structures inside the GNC800 sample, which is due to the slow kinetics of potassiation in graphite. The formations of $KC_8$ and $KC_{24}$ are potential-dependent as compared with the potassiation of bulk graphite.[27] Combined with the discharge curve, we could conclude that $KC_{24}$ is fully formed at a potential of ≈0.12 V. On the other hand, The stage I $KC_8$ forms at potentials from 0.12 to 0 V. When GNC800 is charged to 0.3 V, the peaks of $KC_8$

quickly disappear, and only the $KC_{24}$ peaks can be observed up to a high voltage of 0.7 V. After we charged the battery to a high voltage of 2.0 V, the peaks of $KC_{24}$ could still be detected, which indicates that some dilute potassium ions remain inside the graphite layers in the form of $KC_{24}$. The remaining potassium ions in the carbon skeleton in the form of $KC_{24}$ act as pillars and help retain an enlarged interlayer spacing for the subsequent potassiation (discharge) process.

Raman spectra were simultaneously carried out to detect the structural evolution of GNC800 during (de)potassiation (Figure 6b). When discharged to a lower potential, GNC800 shows decreased $I_D/I_G$ ratios, indicative of the increased disorder and decreased graphene size. A shift of the G peak to high values was observed in the discharge process, in agreement with previous reports.[28] The $I_D/I_G$ ratio increases from 0.3 for the pristine material to eventually a high value of 0.9 for the GNC800 discharged to 0.001 V (Figure 6c), which is a common value for amorphous carbonaceous materials.[49,50] When GNC800 is charged to a 2.0 V, the $I_D/I_G$ ratio is recovered to 0.5, a value still higher than pristine GNC, which suggests that the long-range-ordered structure of GNC800 is irreversibly transformed into a short-range-ordered graphitic structure (Figure S17, Supporting Information). Ex situ XPS was further carried out to detect the potassium ion inside the carbon skeleton at different charge–discharge states (Figure 6d). Discharge makes the C1 s peak broader indicating that more $sp^3$ C—C defects are created during the discharge process, which is in agreement with the ex situ XRD and Raman studies. When GNC800 is charged from 0.001 to 2.0 V, the C 1s peak becomes
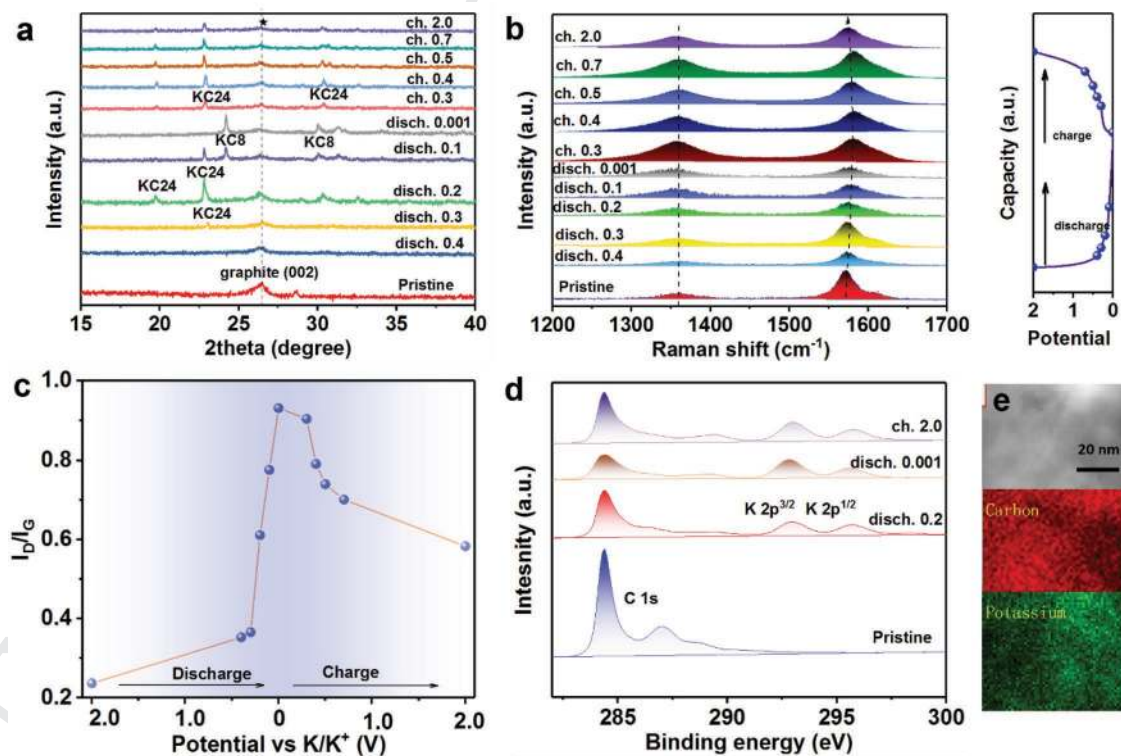


**Figure 6.** The ex situ investigations of GNC800. a) The XRD patterns, b) the Raman spectra with corresponding c) $I_G/I_D$ ratios, d) the C 1s, and K 2p XPS spectra, e) the dark-filed TEM image, and the EDS elemental mapping of fully potassiated GNC800.

sharp, which means that some sp³ disordered structure returns to the sp² ordered state. At 0.2 V, the NGCB shows a C/K ratio of 11 which is lower than $KC_{24}$, suggesting that more K ions are intercalated into the graphite structure. When GNC800 is discharged to 0.001 V, the C/K ratio becomes 6.2, which is lower than $KC_8$. The even distribution of potassium ions in GNC800 is demonstrated by TEM-EDS mapping (Figure 6e). When GNC800 is charged to 2.0 V, the C/K ratio becomes 9.8, which implies that a significant amount of potassium ions remains inside the carbon matrix.[32] Considering the lowest possible C/K ratio is 8 for graphite corresponding to the formation of stage I $KC_8$, the much lower C/K ratio of GNC800 discharged to 0.001 V could originate from the irreversible intercalation of potassium ions, which could be the reason why almost all the carbonaceous anodes face low Coulombic efficiencies within tens of cycles.[51–58] The EDS mappings of carbon and potassium elements demonstrate that there is no phase separation indicating the intercalation mechanism.

Ex situ TEM was further carried out to explore the structural evolution during potassiation and depotassiation process. Pristine GNC800 shows a (002) crystal lattice of 0.340 (**Figure 7**a). When potassiated to 0.2 V, GNC800 electrode displays mixed lattices of 0.340 and 0.386 nm (Figure 7b), which can be indexed to the lattices of graphite and $KC_{24}$, respectively. With further potassiated to 0.001 V, GNC800 shows a lattice of 0.362 nm, which is indexed to $KC_8$. The interlayer spacing of

the discharge product is smaller than that of $KC_8$ formed with a pure graphite precursor, which results in a lower expansion and further high rate capability.[34] It should be noted that the fully potassiated GNC800 shows a distorted, turbostratic, and short-range ordered structure (Figure 7c), which implies that the potassium intercalation in GNC is an omnidirectional potassiation process. When depotassiated to 2.0 V, GNC800 shows an interlayer spacing of 0.340 nm, which is the same with the pristine GNC800. The slightly distorted structure (Figure 7d) indicates that there are some sp³ defects that cannot be recovered, which is the same situation with XRD and Raman study. Based on the above results, the potassium ion storage in defect-rich GNCs is schematically drawn in Figure 7e. The discharge process from 2.0 to 0.36 V corresponds to the dilute potassiation in the defect sites. The discharge from 0.36 to 0.12 V corresponds to the formation of Stage II $KC_{24}$ compound in the graphite layers, and the discharge from 0.12 to 0.001 V is ascribed to the formation of $KC_8$ compound in the graphite layers. The discharge process makes the GNC800 distorted, which creates more active sites for the potassiation process.

Galvanostatic intermittent titration technique and electrochemical impedance spectroscopy (EIS) were further used to investigate the evolution of diffusion coefficient during (de)potassiation process. During both the potassiation and depotassiation processes, GNC600 has a higher $K^+$ diffusion coefficient than GNC700 and GNC800 (Figure S18, Supporting Information),
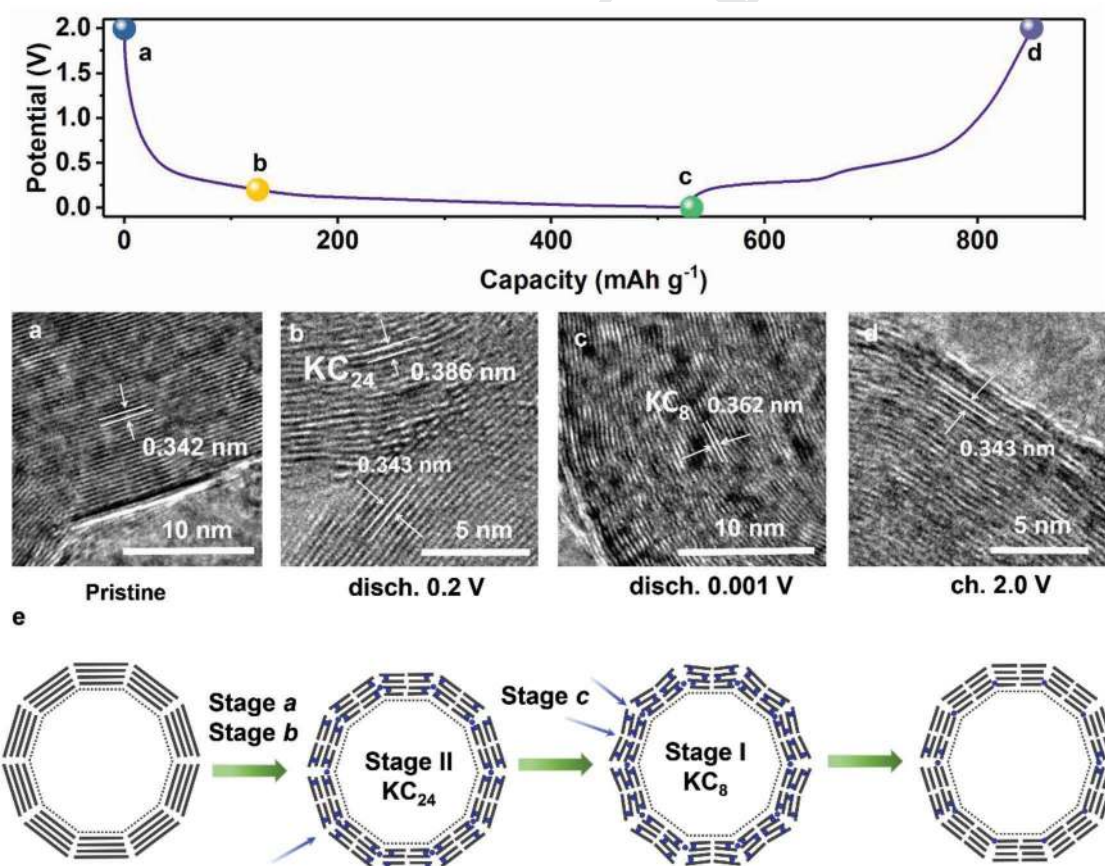


**Figure 7.** a–d) Ex situ TEMs observed at different charge/discharge potentials, e) the below schematic diagram shows the (de)potassiation process and the structural evolution of GNC.

which is because GNC600 contains more defective structures compared with GNC700 and GNC800. In the potassiation process, the diffusion coefficients of GNCs decrease with the discharge process, but slightly increase of diffusion coefficient at low potentials,[59,60] which may be caused by the disordered structures formed in the potassiation process. In the depotassiation process, a higher diffusion coefficient is observed at low potential for both GNCs, which could be the reason that the disordered structures formed at the potassiation process could be beneficial for the deintercalation of potassium ions.

EIS was performed at different charge/discharge potentials to study the evolution of the diffusion coefficient. The EIS spectra were recorded while holding the battery at each potential for 2 h before the measurement (Figure S19a, Supporting Information); this step ensures reaction completion at a certain potential. The EIS results were used to calculate the time constant and further simulated (the equivalent circuit is shown in Figure S19b of the Supporting Information, and the simulated results are shown in Table S4, Supporting Information) to calculate the diffusion coefficient (method shown in Experimental Section S1.4, Supporting Information). In the potassiation process, the charge transfer resistance decreases, and the Warburg diffusion impedance decreases, and finally disappears (Figure S20a, Supporting Information). In the depotassiation process, the Warburg impedance increases and the diffusion coefficient decreases (Figure S20b, Supporting Information). The decreased charge transfer resistance in the potassiation process is due to the disordered structure formation during the potassiation process. The disordered structure provides more active sites for potassium (de)intercalating into the layers of graphite. We calculated the diffusion coefficient based on the EIS results. The diffusion coefficient increases during the potassiation process, and decreases in the depotassiation process (Figure S20c, Supporting Information). The evolution of diffusion coefficient correlates well with the increased degree of disorder ($I_D/I_G$). Thus, we conclude that the defects in the GNCs help build more pathways for the efficient potassiation and the disordered structure formed during the potassiation process, which could enable fast diffusion of potassium ions. The fast diffusion of potassium ions enables a fast potassiation electrode kinetics at low potential range (0–0.2 V), which results in a low time constant (Figure S20d, Supporting Information).

## 3. Conclusion

We have demonstrated a new type of nitrogen-doped, defect-rich GNCs with thin graphitic carbon layers as anodes of potassium ion batteries. Detailed analysis of the potassiation storage mechanism in GNCs shows a clear difference from bulk graphite materials. Specifically, we observe the potential-dependent potassiation in defect-rich GNCs from various directions, which results in the short-range ordered structure of the final discharge product, hence increasing the number of active sites for potassiation and pathways for fast potassium ion diffusion. The optimized GNC600 has high-level nitrogen doping which enables high pseudocapacitive contribution and defect-rich short-range-ordered structure which enables high diffusion coefficient and high rate capability. GNC600 shows better performance than

previously reported thin-walled graphitic carbonaceous materials such as carbon nanocages and nanotubes. These results demonstrate that our strategy is generally effective and can be used in the design of high-performance anodes for KIB.

## 4. Experimental Section

*Preparation of GNCs*: GNCs were prepared from EDTA nickel coordination compound and sodium chloride mixture (denoted as EDTANi·2NaCl). The EDTANi·2NaCl was prepared from a coordination reaction. In a typical synthesis, nickel chloride hexahydrate (23.7 g) was put into deionized water (400 mL) with magnetic stirring to evaporate water and form a grass-green solution, and then EDTA disodium dehydrate (37.2 g) was put into the above solution to form a sky-blue solution. The above solution was further stirred for 10 h at room temperature. Afterward, the sky-blue solution was dried in an 80 °C air-flow oven to form white-blue powders. The white-blue powder, transferred to a porcelain boat, was heat-treated at different temperatures (carbon sample prepared at the temperature of X is denoted as GNCX) in an argon-flow (100 sccm) tube furnace with a ramping rate of 5 °C min$^{-1}$ for 1 h. The pyrolysis product was washed with superfluous 10 wt% HCl aqueous solution at 120 °C for 24 h with circulation reflux of cold water. The as-prepared carbon samples were then filtered with deionized water to a pH value close to 7 and dried overnight at 80 °C.

*Physical Characterization*: The specific surface areas and pore size distributions of GNCs were evaluated by a $N_2$ adsorption/desorption analyzer (ASAP 2420, Micrometrics, USA). SEM images were taken on a scanning electron microscope (Merlin, ZEISS, Germany). TEM images were taken using transmission electron microscope (Titan 80–300 CT, FEI, Thermo Fisher Scientific). XRD patterns were collected on an X-ray diffractometer (D8 Advance, Bruker, Germany) with Cu K$\alpha$ radiation ($\lambda$ = 1.5406 Å). Raman spectra were collected on a micro-Raman spectrometer (LabRAM ARAMIS, Horiba-Jobin Yvon, Germany) using a cobalt laser (473 nm) with a 10% filter. XPS analysis was conducted on photoelectron spectrometer (Kratos Axis Supra, Shimadzu, Japan).

*Electrochemical Characterization*: GNC electrode was prepared by slurry (containing 80 wt% GNC, 10 wt% acetylene black, and 10% sodium carboxymethyl cellulose) casting on copper foil with blade coating technique and dried in a 70 °C vacuum oven for at least 24 h. The electrochemical performance of GNC was evaluated in 2032 coin half-cell, in which GNC and potassium foil were used as working electrode and counter (reference) electrode, respectively. 0.8 mol L$^{-1}$ KPF$_6$ in ethylene carbonate:diethyl carbonate (1:1 by volume) was used as electrolyte. Glass fiber mat (Whatman CAT. No. 1825-047) was used as separator. CV, GCD, and EIS tests were conducted on an electrochemical workstation (VMP3, Biologic, France). Electrochemical impedance spectroscopy was measured in the frequency range from 200 kHz to 10 mHz with a sinusoidal voltage amplitude of 10 mV. All measurements were conducted in ambient condition.

## Supporting Information

Supporting Information is available from the Wiley Online Library or from the author.

## Acknowledgements

## Conflict of Interest

The authors declare no conflict of interest.

## Keywords

anode, defect-rich, graphitic nanocarbon, nano bubble, potassium-ion battery

[1] A. Kwade, W. Haselrieder, R. Leithoff, A. Modlinger, F. Dietrich, K. Droeder, *Nat. Energy* **2018**, *3*, 290.

[2] D. Lin, Y. Liu, Y. Cui, *Nat. Nanotechnol.* **2017**, *12*, 194.

[3] R. Schmuch, R. Wagner, G. Hörpel, T. Placke, M. Winter, *Nat. Energy* **2018**, *3*, 267.

[4] Z. Yang, J. Zhang, M. C. W. Kintner-meyer, X. Lu, D. Choi, J. P. Lemmon, J. Liu, *Chem. Rev.* **2011**, *111*, 3577.

[5] B. Dunn, H. Kamath, J. Tarascon, *Science* **2011**, *334*, 928.

[6] W. Zhang, N. Lin, D. Liu, J. Xu, J. Sha, J. Yin, X. Tan, H. Yang, H. Lu, H. Lin, *Energy* **2017**, *128*, 618.

[7] C. Xia, J. Guo, P. Li, X. Zhang, H. N. Alshareef, *Angew. Chem., Int. Ed.* **2018**, *57*, 3943.

[8] Y. Liang, Y. Jing, S. Gheytani, K. Y. Lee, P. Liu, A. Facchetti, Y. Yao, *Nat. Mater.* **2017**, *16*, 841.

[9] H. Tian, T. Gao, X. Li, X. Wang, C. Luo, X. Fan, C. Yang, L. Suo, Z. Ma, W. Han, C. Wang, *Nat. Commun.* **2017**, *8*, 14083.

[10] W. Chen, G. Li, A. Pei, Y. Li, L. Liao, H. Wang, J. Wan, Z. Liang, G. Chen, H. Zhang, J. Wang, Y. Cui, *Nat. Energy* **2018**, *3*, 428.

[11] C. Bommier, D. Mitlin, X. Ji, *Prog. Mater. Sci.* **2018**, *97*, 170.

[12] C. Delmas, *Adv. Energy Mater.* **2018**, *8*, 1703137.

[13] D. Saurel, B. Orayech, B. Xiao, D. Carriazo, X. Li, T. Rojo, *Adv. Energy Mater.* **2018**, *8*, 1703268.

[14] C. Vaalma, D. Buchholz, M. Weil, S. Passerini, *Nat. Rev. Mater.* **2018**, *3*, 18013.

[15] J. C. Pramudita, D. Sehrawat, D. Goonetilleke, N. Sharma, *Adv. Energy Mater.* **2017**, *7*, 1602911.

[16] S. Komaba, W. Murata, T. Ishikawa, N. Yabuuchi, T. Ozeki, T. Nakayama, A. Ogata, K. Gotoh, K. Fujiwara, *Adv. Funct. Mater.* **2011**, *21*, 3859.

[17] H. Kim, J. C. Kim, M. Bianchini, D. H. Seo, J. Rodriguez-Garcia, G. Ceder, *Adv. Energy Mater.* **2018**, *8*, 1702384.

[18] Y. H. Zhu, X. Yang, D. Bao, X. F. Bie, T. Sun, S. Wang, Y. S. Jiang, X. B. Zhang, J. M. Yan, Q. Jiang, *Joule* **2018**, *2*, 736.

[19] K. Chihara, A. Katogi, K. Kubota, S. Komaba, *Chem. Commun.* **2017**, *53*, 5208.

[20] P. Xiong, X. Zhao, Y. Xu, *ChemSusChem* **2018**, *11*, 202.

[21] Y. Liu, F. Fan, J. Wang, Y. Liu, H. Chen, K. L. Jungjohann, Y. Xu, Y. Zhu, D. Bigio, T. Zhu, C. Wang, *Nano Lett.* **2014**, *14*, 3445.

[22] S. Komaba, T. Hasegawa, M. Dahbi, K. Kubota, *Electrochem. Commun.* **2015**, *60*, 172.

[23] W. Luo, J. Wan, B. Ozdemir, W. Bao, Y. Chen, J. Dai, H. Lin, Y. Xu, F. Gu, V. Barone, L. Hu, *Nano Lett.* **2015**, *15*, 7671.

[24] Z. Jian, Z. Xing, C. Bommier, Z. Li, X. Ji, *Adv. Energy Mater.* **2016**, *6*, 1501847.

[25] D. S. Bin, Z. X. Chi, Y. Li, K. Zhang, X. Yang, Y. G. Sun, J. Y. Piao, A. M. Cao, L. J. Wan, *J. Am. Chem. Soc.* **2017**, *139*, 13492.

[26] D. A. Stevens, J. R. Dahn, *J. Electrochem. Soc.* **2001**, *148*, A803.

[27] Z. Jian, W. Luo, X. Ji, *J. Am. Chem. Soc.* **2015**, *137*, 11566.

[28] K. Share, A. P. Cohn, R. E. Carter, C. L. Pint, *Nanoscale* **2016**, *8*, 16435.

[29] A. P. Cohn, N. Muralidharan, R. Carter, K. Share, L. Oakes, C. L. Pint, *J. Mater. Chem. A* **2016**, *4*, 14954.

[30] Y. Wang, Z. Wang, Y. Chen, H. Zhang, M. Yousaf, H. Wu, M. Zou, A. Cao, R. P. S. Han, *Adv. Mater.* **2018**, *30*, 1802074.

[31] M. Chen, W. Wang, X. Liang, S. Gong, J. Liu, Q. Wang, S. Guo, H. Yang, *Adv. Energy Mater.* **2018**, *8*, 1800171.

[32] W. Wang, J. Zhou, Z. Wang, L. Zhao, P. Li, Y. Yang, C. Yang, H. Huang, S. Guo, *Adv. Energy Mater.* **2018**, *8*, 1701648.

[33] B. Cao, Q. Zhang, H. Liu, B. Xu, S. Zhang, T. Zhou, J. Mao, W. K. Pang, Z. Guo, A. Li, J. Zhou, X. Chen, H. Song, *Adv. Energy Mater.* **2018**, *8*, 1801149.

[34] L. Wang, J. Yang, J. Li, T. Chen, S. Chen, Z. Wu, J. Qiu, B. Wang, P. Gao, X. Niu, H. Li, *J. Power Sources* **2019**, *409*, 24.

[35] D. S. Bin, X. J. Lin, Y. G. Sun, Y. S. Xu, K. Zhang, A. M. Cao, L. J. Wan, *J. Am. Chem. Soc.* **2018**, *140*, 7127.

[36] Y. Xu, C. Zhang, M. Zhou, Q. Fu, C. Zhao, M. Wu, Y. Lei, *Nat. Commun.* **2018**, *9*, 1720.

[37] W. Zhang, J. Zhu, H. Ang, Y. Zeng, N. Xiao, Y. Gao, W. Liu, H. H. Hng, Q. Yan, *Nanoscale* **2013**, *5*, 9651.

[38] K. Share, A. P. Cohn, R. Carter, B. Rogers, C. L. Pint, *ACS Nano* **2016**, *10*, 9738.

[39] Y. Liu, J. S. Xue, T. Zheng, J. R. Dahn, *Carbon* **1996**, *34*, 193.

[40] Y. Xie, Y. Chen, L. Liu, P. Tao, M. Fan, N. Xu, X. Shen, C. Yan, *Adv. Mater.* **2017**, *29*, 1702268.

[41] Y. Liu, C. Yang, Q. Pan, Y. Li, G. Wang, X. Ou, F. Zheng, X. Xiong, M. Liu, Q. Zhang, *J. Mater. Chem. A* **2018**, *6*, 15162.

[42] X. Lin, J. Huang, B. Zhang, *Carbon* **2019**, *143*, 138.

[43] A. Mahmood, S. Li, Z. Ali, H. Tabassum, B. Zhu, Z. Liang, W. Meng, W. Aftab, W. Guo, H. Zhang, M. Yousaf, S. Gao, R. Zou, Y. Zhao, *Adv. Mater.* **2018**, *30*, 1805430.

[44] P. Bai, Y. He, X. Zou, X. Zhao, P. Xiong, Y. Xu, *Adv. Energy Mater.* **2018**, *8*, 1703217.

[45] S. Qiu, L. Xiao, M. L. Sushko, K. S. Han, Y. Shao, M. Yan, X. Liang, L. Mai, J. Feng, Y. Cao, X. Ai, H. Yang, J. Liu, *Adv. Energy Mater.* **2017**, *7*, 1700403.

[46] Z. Li, C. Bommier, Z. Sen Chong, Z. Jian, T. W. Surta, X. Wang, Z. Xing, J. C. Neuefeind, W. F. Stickle, M. Dolgos, P. A. Greaney, X. Ji, *Adv. Energy Mater.* **2017**, *7*, 1602894.

[47] H. Lu, F. Ai, Y. Jia, C. Tang, X. Zhang, Y. Huang, H. Yang, Y. Cao, *Small* **2018**, *14*, 1802694.

[48] C. Bommier, T. W. Surta, M. Dolgos, X. Ji, *Nano Lett.* **2015**, *15*, 5888.

[49] W. Zhang, Y. Lei, F. Ming, Q. Jiang, P. M. F. J. Costa, H. N. Alshareef, *Adv. Energy Mater.* **2018**, *8*, 1801840.

[50] X. Zhao, P. Xiong, J. Meng, Y. Liang, J. Wang, Y. Xu, *J. Mater. Chem. A* **2017**, *5*, 19237.

[51] Z. Ju, P. Li, G. Ma, Z. Xing, Q. Zhuang, Y. Qian, *Energy Storage Mater.* **2018**, *11*, 38.

[52] G. Ma, K. Huang, J. S. Ma, Z. Ju, Z. Xing, Q. C. Zhuang, *J. Mater. Chem. A* **2017**, *5*, 7854.

[53] J. Zhao, X. Zou, Y. Zhu, Y. Xu, C. Wang, *Adv. Funct. Mater.* **2016**, *26*, 8103.

[54] J. Yang, Z. Ju, Y. Jiang, Z. Xing, B. Xi, J. Feng, S. Xiong, *Adv. Mater.* **2018**, *30*, 1700104.

[55] X. Qi, K. Huang, X. Wu, W. Zhao, H. Wang, Q. Zhuang, Z. Ju, *Carbon* **2018**, *131*, 79.

[56] X. Zhao, Y. Tang, C. Ni, J. Wang, A. Star, Y. Xu, *ACS Appl. Energy Mater.* **2018**, *1*, 1703.

[57] C. Chen, Z. Wang, B. Zhang, L. Miao, J. Cai, L. Peng, Y. Huang, J. Jiang, Y. Huang, L. Zhang, J. Xie, *Energy Storage Mater.* **2017**, *8*, 161.

[58] Z. Xing, Y. Qi, Z. Jian, X. Ji, *ACS Appl. Mater. Interfaces* **2017**, *9*, 4343.

[59] Z. Jian, Z. Xing, C. Bommier, Z. Li, X. Ji, *Adv. Energy Mater.* **2016**, *6*, 1501874.

[60] Z. Li, Y. Chen, Z. Jian, H. Jiang, J. J. Razink, W. F. Stickle, J. C. Neuefeind, X. Ji, *Chem. Mater.* **2018**, *30*, 4536.